Article

Subwavelength Chiral Spiral Acoustic Metamaterials for a Robust Topological Acoustic Insulator

Tao Yang [1,2]**, Meng Chen** [1,2,]*****, Boya Xiao** [1,2]**, Yu Liu** [1,2]**, Heng Jiang** [1,2,]***** **and Yuren Wang** [1,2]

1   Key Laboratory of Microgravity, Institute of Mechanics, Chinese Academy of Sciences, Beijing 100190, China; yangtao1@imech.ac.cn (T.Y.); xiaoboya@imech.ac.cn (B.X.); liuyu@imech.ac.cn (Y.L.); yurenwang@imech.ac.cn (Y.W.)
2   University of Chinese Academy of Sciences, Beijing 100049, China
*   Correspondence: chenmeng@imech.ac.cn (M.C.); hengjiang@imech.ac.cn (H.J.)

Abstract: Topological acoustic insulators enable sound waves to transmit along the surface without backscattering, which builds a new pathway towards sound wave control. However, a large share of topological acoustic insulators are realized based on special point group symmetry and Bragg scattering mechanism. This method not only exerts a restriction on the unit cell design but also requires the lattice constant to be comparable with the wavelength. In this paper, the chiral spiral acoustic metamaterials are constructed based on an Archimedean spiral structure. This structure enjoys subwavelength characteristics and is easy to construct. Taking advantage of the chirality of the spiral structure topological phases with opposite energy flow direction can be constructed. The edge state is formed at the interface composed of the spiral units sharing different chirality, which does not depend on point group symmetry. The topological transportation on the interfaces shows strong robustness despite sharp corners verified by straight and zigzag waveguides. The topological acoustic insulator with a chiral spiral structure provides a novel strategy for small acoustic devices with robust sound transmission.

Keywords: chiral spiral structure; acoustic metamaterials; topological transportation

1. Introduction

Inspired by the topological insulators [1,2] in condensed matter physics, the analogous topological insulators in acoustic realm have received significant interest. The edge state characterized by the one-way transmission without backscattering lays a new pathway for acoustic wave guiding, which enables the acoustic wave to propagate robustly along the surface or edge being immune to the defects. By emulating the quantum Hall effect (QHE) [3,4], quantum spin Hall effect (QSHE) [5,6], and quantum Valley Hall effect (QVHE) [7,8] in electronic systems, similar topological transmission is also realized in classical acoustic systems [9–15]. The researchers [16–18] introduced the circulating fluid into the ring resonator, mimicking the magnetic field in an electronic system, and realized the analogue QHE. Some topological acoustic systems [19–21] realize the analogue QSHE by adjusting the filling ratio within the hexagonal honeycomb lattice to realize inversion of the acoustic energy band at a double Dirac cone. In addition, researchers [22–26] also broke the inversion symmetry of the structure by rotating the scatterer, making the Dirac point at the K point in the Brillouin zone split, giving rise to different Valley hall phases, thus realizing the analogue QVHE.

Although these topological acoustic systems have achieved a great milestone, most of them depend on the special point group symmetry. In this way, a Dirac cone forms at the high symmetry point in the Brillouin zone, and then the reduced symmetry of the unit cell contributes to the Dirac cone split through rotation, scaling and other operations, giving rise to different topological phases. Thus, the interfaces composed of different topological phases hold the one-way transmission edge states. Furthermore, a large share of these

schemes are based on the Bragg scattering mechanism, which requires the unit cell size to be comparable with the wavelength, so it is difficult to bring the benefit to the miniaturization of a topological acoustic system. Although some systems at deep-subwavelength scale have been reported based on local resonance [27,28], the structures of this are relatively complicated. On the other hand, the topological transmission of these systems also depends on special point group symmetry, which exerts some restrictions on the unit cell design.

In acoustic metamaterials, the spiral structure [29–32] featuring space-coiling creates a lengthy sound channel within a small space resulting in low-frequency resonant mode, and the whole structure possesses subwavelength characteristics. Compared with the labyrinthine space-coiling structure, the spiral structure is much simpler, and can meet the requirement of the subwavelength topological system. In addition, the topological interfaces in the valley Hall system are formed by distinct valley phases with opposite energy flow chirality. Therefore, opposite chiral structural units can be used to artificially generate topological phases with opposite energy flow chirality, and the interface composed of opposite chiral structural units will hold the edge states. In view of this, particular point group symmetry is not necessary for the generation of edge states [33,34].

In this work, we design a topological acoustic system based on a subwavelength chiral spiral acoustic metamaterial. Due to the space folding scheme, the lengthy sound channel contributes to the subwavelength characteristics. The band gap can be reduced to the subwavelength frequency range. Furthermore, the whole system is composed of a chiral spiral structure, which does not rely on special point group symmetry. Compared with other topological systems based on QVHE, in this paper the whole system depends on the chiral symmetry. In addition, the unit cell is designed based on the Archimedean spiral, which is simpler than the space-folding structure. The length of the sound channel within the spiral unit cell can be changed by adjusting the number of turns of the spiral, so that the eigenfrequency of the unit cell can be lowered down and the subwavelength property is realized. Furthermore, since the spiral structure shares left-handed and right-handed chirality, opposite chiral structural units can be used to artificially generate topological phases with opposite energy flow chirality. The interfaces composed of opposite chiral structural units will hold the edge state. The topological edge state protected by chiral symmetry is also robust to defects, which provides a new pathway towards the design of acoustic devices.

2. Structure Design

The left-handed Archimedean spiral structure is shown in Figure 1a. The spiral equation is $r(s) = R - (R - r)s$, $\phi(s) = 2\pi ns$, where R is the outer radius of the Archimedean spiral, r is the inner radius of the spiral, n is the number of turns of the spiral, and $s \in [0; 1]$, and w is the width of the spiral. The whole spiral structure is considered as the scatterer distributed in the honeycomb unit cell filled with air, shown in Figure 1b. The geometric parameters of the spiral are: the inner radius of the spiral $r = 0.3$ cm, the outer radius $R = 1.2$ cm, the number of turns of the spiral $n = 2$, the width of the spiral $w = 0.1$ cm, and the lattice constant $a = 4$ cm. The material parameters are as follows: steel spiral structure (mass density $\rho_1 = 7700$ kg/m^3, sound velocity $c_1 = 5400$ m/s), and the gray air area (mass density $\rho_0 = 1.29$ kg/m^3, sound velocity $c_0 = 340$ m/s).
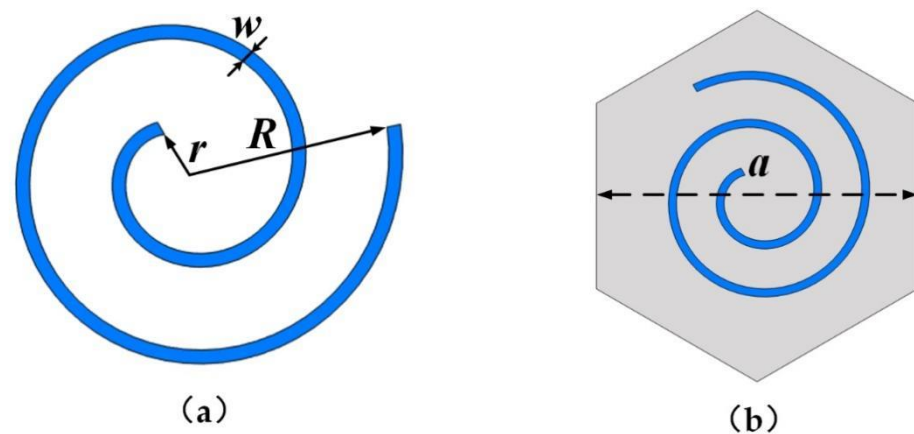
Figure 1. (**a**) Schematic of an Archimedean spiral with its geometric parameters. (**b**) The left-handed spiral distributed in honeycomb unit cell.

3. Results

3.1. Band Structure

Employing the finite element software COMSOL Multiphysics to calculate the band structure of spiral metamaterials. Note that the whole metamaterial is a periodic structure, and the Floquet Bloch periodic conditions are imposed on the boundaries of the unit cell. Along the boundary of the first Brillouin zone, M-Γ-K-M scanning wave vector is adopted to obtain the energy band of the whole structure. The band structure is shown in Figure 2a, where $f_c = c_0/a$. There exist three band gaps during the normalized frequency range of 0–0.6: the first band gap (0.117–0.141), the second band gap (0.354–0.371), and the third band gap (0.498–0.528). Among them, the first and the second band gaps are the local resonant band gap thanks to the lengthy spiral design, whose normalized frequency is less than 0.5. The third band gap is the Bragg scattering band gap owing to the symmetry-broken, which forms the band gap at the high symmetry point K. To better understand these three band gaps, the eigenmodes of the four energy bands corresponding to the K point in the Brillouin region are analyzed. These four eigenmodes are labeled as 1, 2, 3, and 4, respectively, and the corresponding normalized frequencies are 0.117 (994 Hz), 0.35 (2975 Hz), 0.496 (4218 Hz), and 0.535 (4545 Hz), respectively. Figure 2b shows the eigenmodes of each energy band. It suggests that the first and the second eigenmodes are excited by the local resonance effect since the resonance part is mainly distributed in the spiral structure. The third and the fourth eigenmodes are excited by the Bragg scattering effect since the resonance part is mainly distributed outside the spiral structure. The eigenmodes of the left-handed and right-handed structures corresponding to each band are mirror symmetric. It can be concluded that the spiral structure can effectively lower the whole system frequency, which possesses the subwavelength characteristics.

Next, we investigated the effect of the geometric parameters on the band gaps. First, we rotated the spiral structure around the center of the unit cell, which can be characterized by θ. Figure 3a shows the variation of the first, second and third band gap widths with the rotation angle θ, marked by grey, blue, and orange areas, respectively. It can be derived from the figure that the rotation angle θ hardly affects the first and second band gaps, but has a certain effect on the third band gap. This is because the first and second band gaps are formed by the local resonance effect of the spiral structure which is bound to the length of the spiral, and the change of the rotation angle hardly affects their eigenfrequency. The third band gap is formed by the Bragg scattering effect. Therefore, the variation of rotation angle will change the unit cell symmetry, and the eigenfrequency will be influenced by the rotation angle. It can be seen that when the rotation angle is 70°, the third band gap is the narrowest.
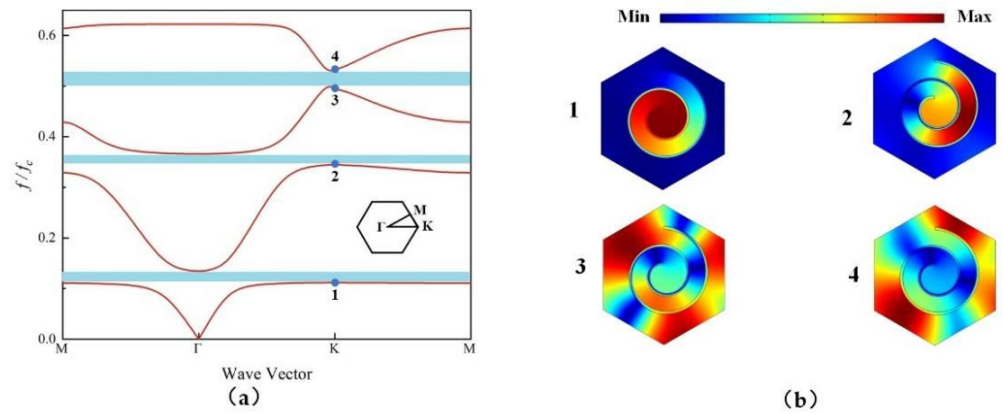
Figure 2. (**a**) The band structure of the left-handed spiral structure with *n* = 2. (**b**) Eigenmodes at K point in Brillouin zone corresponding to four energy bands.
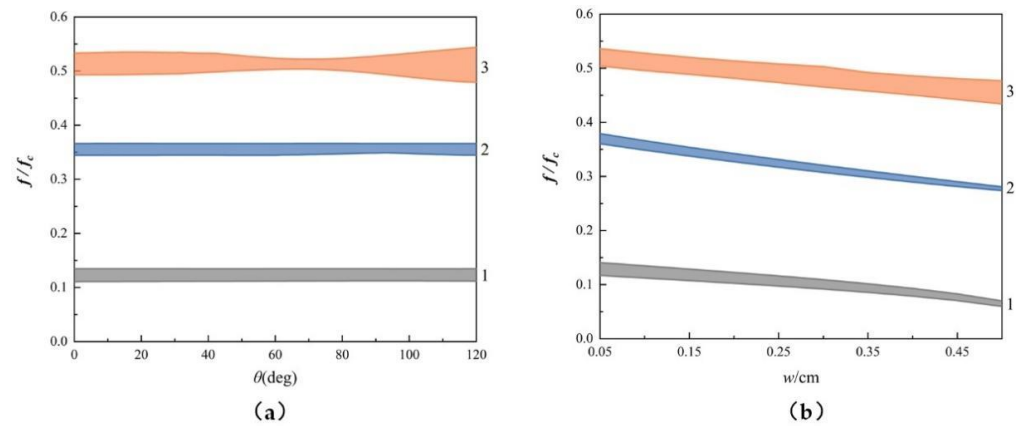

Figure 3. The first, second and third band gap varies with geometric parameters marked by grey, blue, and orange areas, respectively. (**a**) Rotation angle θ ranging from $0°$ to $120°$. (**b**) Width of spiral *w* ranging from 0.05 cm to 0.5 cm.

To explore the effect of width of spiral *w* on the band gaps, the rotation angle is set to $\theta = 0°$. Figure 3b shows the variation of the first, second and third band gap widths with the width of spiral *w* ranging from 0.05 cm to 0.5 cm, marked by grey, blue, and orange areas, respectively. From the diagram, with the increase of the width of the spiral, the frequency of the first, second and third band gap decreases gradually, indicating that the local resonance effect is enhanced. Furthermore, the width of the first and second band gaps decreases with the increase of the spiral width, and the width of the third band gap is less affected by the spiral width.

Then, the number of turns of the spiral *n* is changed to explore its effect on the energy band. Figure 4 shows the energy band of the spiral structure with a different number of turns *n*, where the *n* = 1, 1.5, and 2, respectively. It can be derived that the frequency of the first band gap decreases with the increase of the number of turns, which is owing to the length extension of the spiral structure. In this way, the frequency of the first resonant mode decreases. Moreover, with the increase of *n*, the number of local resonant modes increases, which generates new energy bands and band gaps. When *n* = 2, there are two dispersion curves and two local resonant band gaps below 0.5 the normalized frequency. In the band diagram, there always exists tiny gaps around the reduced frequency 0.55 at K point, whatever the value of n. It reveals that the tiny gap is owed to the Bragg Scattering mechanism, which doesn't show the subwavelength property.
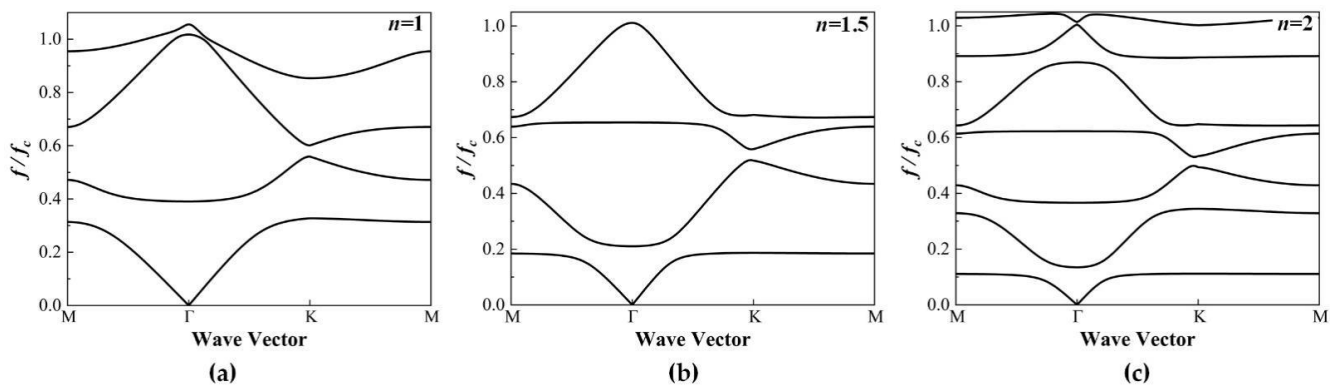
Figure 4. The energy band of the spiral structure with the number of turns *n* = 1, 1.5, and 2.

For the spiral structure with *n* = 2, we explore the topological characteristics of the first, second and third band gaps by calculating the Berry curvature of the first, second, third and fourth energy bands in the first Brillouin zone. The topological properties of the band gap can be characterized by the topological properties of the upper and lower band of the band gap. We calculate the Berry curvature $\Omega = \int i\nabla_k \times u(k)|\nabla_k|u(k)\mathrm{d}k^2$ through the numerical method [35]. The calculated Berry curvature of the first, second, third and fourth energy bands is shown in Figure 5. From the Berry curvature distribution, the first and second energy bands are topological trivial since the Berry curvature across the whole Brillouin zone is 0. The third and fourth energy bands are topological non-trivial since there exist extrema near the K, K′ point in the Berry curvature distribution, which is protected by the valley topology. Therefore, the first band gap between the first and second energy bands is the topological trivial band gap, indicating no topological edge state. The second band gap between the second and third energy bands is a topological non-trivial local resonant band gap, which promises the existence of a topological edge state. The third band gap between the third and fourth energy bands is a topological non-trivial Bragg scattering band gap, which also holds the topological edge state.
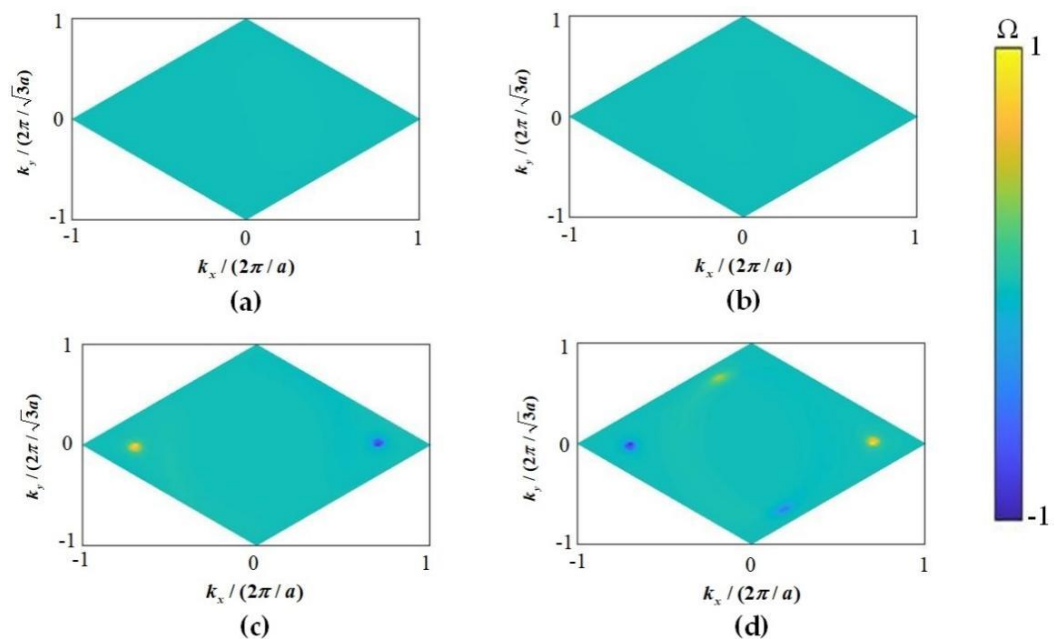

Figure 5. Berry curvature over the first Brillouin zone for each energy band of the spiral structure. (**a**) The first band (**b**) The second band (**c**) The third band (**d**) The fourth band.

To construct the topological edge state with different chiral spiral units, we have calculated the Valley Chern numbers for different chirality. The Valley Chern numbers of the third band are calculated by integrating the Berry curvature over a finite square around the K point. The side length of the finite square is $\frac{\pi}{a}$, k_x ranges from $\frac{5\pi}{6a}$ to $\frac{11\pi}{6a}$ and k_y ranges from $-\frac{\pi}{2a}$ to $\frac{\pi}{2a}$. Figure 6 shows the Valley Chern numbers of the left-handed and right-handed spiral, respectively. The Valley Chern number of a left-handed spiral is 0.2, shown in Figure 6a, and the right-handed spiral is -0.2, shown in Figure 6b.
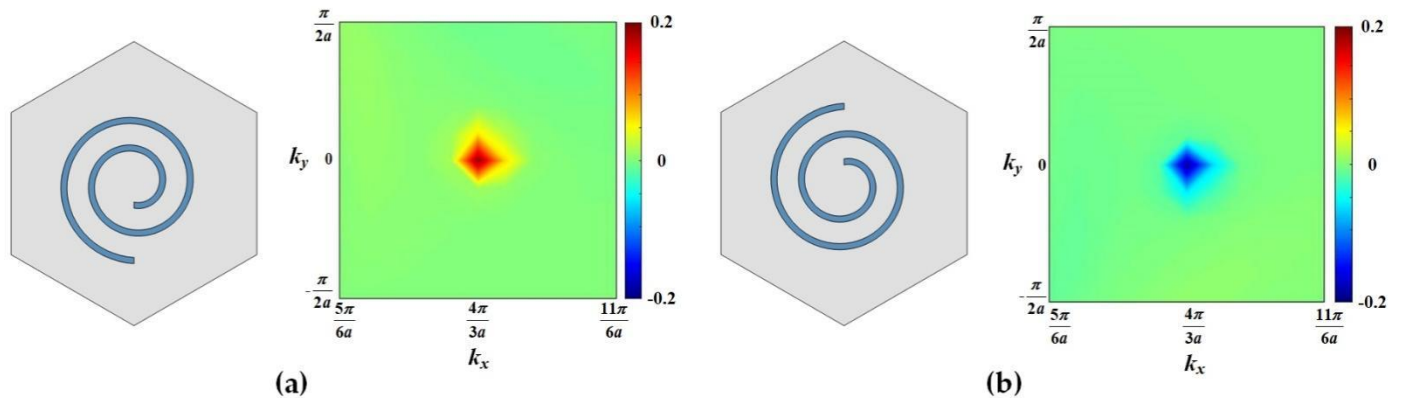

Figure 6. Valley Chern numbers of the third band around K point. k_x ranges from $\frac{5\pi}{6a}$ to $\frac{11\pi}{6a}$ and k_y ranges from $-\frac{\pi}{2a}$ to $\frac{\pi}{2a}$. (**a**) The left-handed spiral. (**b**) The right-handed spiral.

3.2. Topological Edge States

In order to verify the existence of topological edge states, a ribbon-shaped superlattice in 14a × a is constructed, as shown in Figure 7a. The superlattice is composed of seven left-handed spiral units and seven right-handed spiral units, and an interface between them is marked by red lines. The right-handed spiral structure is located above the interface, and the left-handed spiral structure is situated below the interface. In calculation, the periodic boundary condition is imposed along the left and right boundary of the superlattice. The projected energy band of the superlattice in k_x direction is shown in Figure 7b. The grey and red curve is the energy diagram representing the bulk state and the edge state, respectively. The edge states only exist in the second and third band gap, which don't own the subwavelength property. Figure 7c shows the pressure and intensity field on the interface for the edge mode located in the second band gap when $k_x = 0.6\,\pi/a$. We can find that the sound pressure field is mainly confined at the interface and decays exponentially towards the bulk lattice. From the direction of energy flow, it can be derived that the energy flow propagates to the right along the interface, which is in the same direction as the wave vector.

In addition, the existence of topological edge states in the k_y direction is also verified by a ribbon-shaped superlattice in 14a × a, shown in Figure 8a. The projected energy band of the superlattice in k_y direction is shown in Figure 8b. The grey and red curve in the energy diagram represent the bulk state and the edge state, respectively. Figure 8c shows the pressure and intensity field on the interface for the edge mode located in the second band gap when $k_y = \pi/(\sqrt{3}a)$. We can also find that the edge states exist in the k_y direction.

According to the above analysis, the interfaces composed of spiral units sharing different chirality support the edge state. In order to show the transportation of the edge state, a straight waveguide in 18a × 20a lattice composed of left-handed and right-handed spiral units is constructed, as shown in Figure 9a. Sound waves are emitted from the left side. It can be seen from Figure 9a that the sound waves propagate to the right side along the straight interface at 3130 Hz within the second band gap and decays exponentially towards the bulk of the metamaterial. Next, to test the robustness of the edge states, defects are introduced into the interface. In Figure 9b, a sharp corner is introduced in the zigzag

interface. It also shows that the edge states can propagate stably along the zigzag interface, which confirms the robustness of the edge states protected by the chirality.
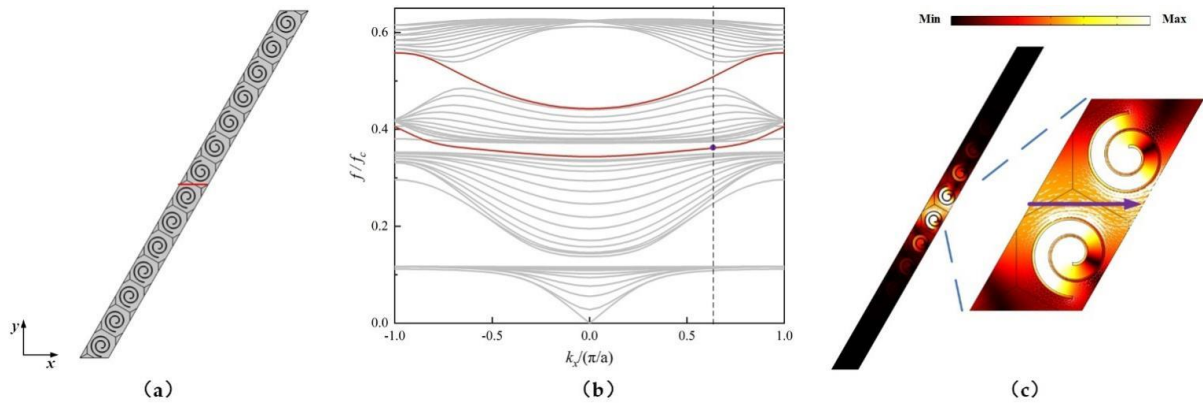

Figure 7. (**a**) The ribbon-shaped superlattice in 14a $\times$ a composed of left-handed and right-handed spiral units. (**b**) The projected band structure of the superlattice in the k_x direction; the edge state and bulk state are represented by the red curve and gray curve, respectively. (**c**) The pressure and intensity field on the interface for the edge states of the second band gap with $k_x = 0.6\pi/a$. The purple arrow represents the direction of the energy flow.
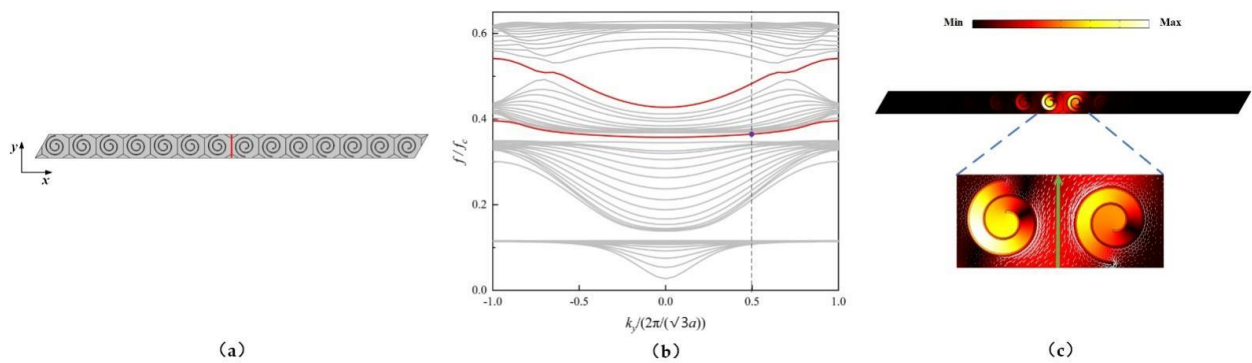

Figure 8. (**a**) The ribbon-shaped superlattice in a$\times$14a composed of left-handed and right-handed spiral units. (**b**) The projected band structure of the superlattice in the k_y direction, the edge state and bulk state are represented by the red curve and gray curve, respectively. (**c**) The pressure and intensity field on the interface for the edge states of the second band gap with $k_y = \pi/(\sqrt{3}a)$. The green arrow represents the direction of the energy flow.
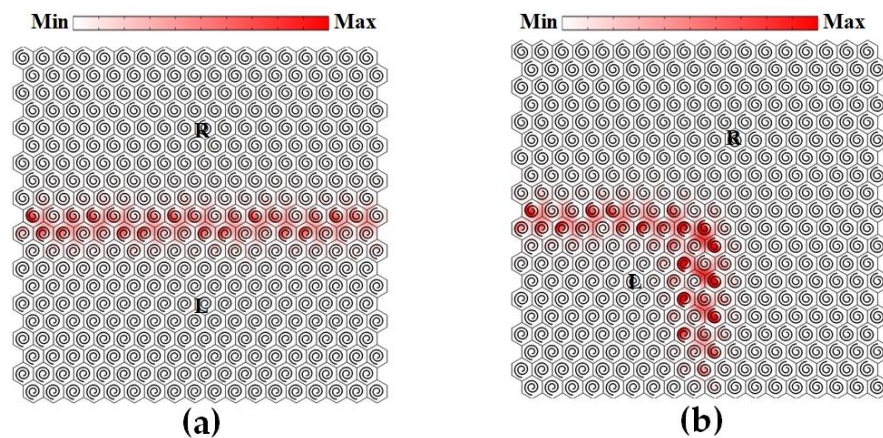

Figure 9. Transmitted edge states through different waveguide configuration (**a**) straight waveguide and (**b**) zigzag waveguide at 3130 Hz.

4. Conclusions

In this paper, a chiral spiral acoustic topological insulator based on the Archimedean spiral scheme is proposed. The topological system does not depend on point group symmetry, and the spiral unit cell enjoys subwavelength characteristics which can effectively lower down the eigenfrequency of the system. The effect of geometric parameters of the spiral structure on the band gap is studied. It suggests that the rotation angle θ only affects the third band gap and has little effect on the first and second band gaps. The frequency of the band gap decreases with the increase of spiral width w, and the first and second band gaps gradually become narrow. The increase of the number of turns n will not only lower the frequency of the first resonant mode, but also introduce more eigenmodes, giving rise to new dispersion curves in band structure. According to the calculated Berry curvature, it is found that the first band gap is a topological trivial local resonant band gap, the second band gap is a topological non-trivial local resonant band gap, and the third band gap is a topological non-trivial Bragg scattering topological band gap. The interfaces composed of left-handed and right-handed spiral units confirm the existence of the edge state protected by chirality. Based on this, the straight and zigzag waveguide is constructed, and the edge states show strong robustness for the propagation at the topological interfaces. Our study reveals that the valley states do not strongly rely on the point group symmetry, since the chiral scheme can also generate a topological transition. This strategy lays a new pathway for the design of topological systems.

References

1. Hasan, M.Z.; Kane, C.L. Colloquium: Topological insulators. *Rev. Mod. Phys.* **2010**, *82*, 3045–3067. [CrossRef]
2. Qi, X.; Zhang, S. Topological insulators and superconductors. *Rev. Mod. Phys.* **2011**, *83*, 1057–1110. [CrossRef]
3. Klitzing, K.V.; Dorda, G.; Pepper, M. New Method for High-Accuracy Determination of the Fine-Structure Constant Based on Quantized Hall Resistance. *Phys. Rev. Lett.* **1980**, *45*, 494–497. [CrossRef]
4. Laughlin, R.B. Anomalous Quantum Hall Effect: An Incompressible Quantum Fluid with Fractionally Charged Excitations. *Phys. Rev. Lett.* **1983**, *50*, 1395–1398. [CrossRef]
5. Kane, C.L.; Mele, E.J. Quantum Spin Hall Effect in Graphene. *Phys. Rev. Lett.* **2005**, *95*, 226801. [CrossRef] [PubMed]
6. Bernevig, B.A.; Zhang, S.C. Quantum spin Hall effect. *Phys. Rev. Lett.* **2006**, *96*, 106802. [CrossRef]
7. Yao, W.; Xiao, D.; Niu, Q. Valley-dependent optoelectronics from inversion symmetry breaking. *Phys. Rev. B* **2008**, *77*, 235406. [CrossRef]
8. Ju, L.; Shi, Z.; Nair, N.; Lv, Y.; Jin, C.; Velasco, J.; Ojeda-Aristizabal, C.; Bechtel, H.A.; Martin, M.C.; Zettl, A.; et al. Topological valley transport at bilayer graphene domain walls. *Nature* **2015**, *520*, 650–655. [CrossRef]
9. Zhang, X.; Xiao, M.; Cheng, Y.; Lu, M.; Christensen, J. Topological sound. *Commun. Phys.* **2018**, *1*, 97. [CrossRef]
10. Pirie, H.; Sadhuka, S.; Wang, J.; Andrei, R.; Hoffman, J.E. Topological Phononic Logic. *Phys. Rev. Lett.* **2022**, *128*, 015501. [CrossRef]
11. Wen, Z.; Zeng, S.; Wang, D.; Jin, Y.; Djafari-Rouhani, B. Robust edge states of subwavelength chiral phononic plates. *Extrem. Mech. Lett.* **2021**, *44*, 101209. [CrossRef]
12. Qiu, H.; Xiao, M.; Zhang, F.; Qiu, C. Higher-Order Dirac Sonic Crystals. *Phys. Rev. Lett.* **2021**, *127*, 146601. [CrossRef] [PubMed]
13. Yang, Z.; Peng, Y.; Li, X.; Zou, X.; Cheng, J. Boundary-dependent corner states in topological acoustic resonator array. *Appl. Phys. Lett.* **2020**, *117*, 113501. [CrossRef]

14. Wang, Y.; Dong, Y.; Zhai, S.; Ding, C.; Luo, C.; Zhao, X. Reconfigurable topological transition in acoustic metamaterials. *Phys. Rev. B* **2020**, *102*, 174107. [CrossRef]

15. Zheng, S.; Duan, G.; Xia, B. Progress in Topological Mechanics. *Appl. Sci.* **2022**, *12*, 1987. [CrossRef]

16. Fleury, R.; Sounas, D.L.; Sieck, C.F.; Haberman, M.R.; Alù, A. Sound Isolation and Giant Linear Nonreciprocity in a Compact Acoustic Circulator. *Science* **2014**, *343*, 516–519. [CrossRef] [PubMed]

17. Khanikaev, A.B.; Fleury, R.; Mousavi, S.H.; Alù, A. Topologically robust sound propagation in an angular-momentum-biased graphene-like resonator lattice. *Nat. Commun.* **2015**, *6*, 8260. [CrossRef] [PubMed]

18. Ding, Y.; Peng, Y.; Zhu, Y.; Fan, X.; Yang, J.; Liang, B.; Zhu, X.; Wan, X.; Cheng, J. Experimental Demonstration of Acoustic Chern Insulators. *Phys. Rev. Lett.* **2019**, *122*, 014302. [CrossRef]

19. He, C.; Ni, X.; Ge, H.; Sun, X.-C.; Chen, Y.-B.; Lu, M.-H.; Liu, X.-P.; Chen, Y.-F. Acoustic topological insulator and robust one-way sound transport. *Nat. Phys.* **2016**, *12*, 1124–1129. [CrossRef]

20. Zhang, Z.; Wei, Q.; Cheng, Y.; Zhang, T.; Wu, D.; Liu, X. Topological Creation of Acoustic Pseudospin Multipoles in a Flow-Free Symmetry-Broken Metamaterial Lattice. *Phys. Rev. Lett.* **2017**, *118*, 084303. [CrossRef]

21. Deng, Y.; Ge, H.; Tian, Y.; Lu, M.; Jing, Y. Observation of zone folding induced acoustic topological insulators and the role of spin-mixing defects. *Phys. Rev. B* **2017**, *96*, 184305. [CrossRef]

22. Lu, J.; Qiu, C.; Ye, L.; Fan, X.; Ke, M.; Zhang, F.; Liu, Z. Observation of topological valley transport of sound in sonic crystals. *Nat. Phys.* **2016**, *13*, 369–374. [CrossRef]

23. Xie, B.; Liu, H.; Cheng, H.; Liu, Z.; Tian, J.; Chen, S. Dirac points and the transition towards Weyl points in three-dimensional sonic crystals. *Light Sci. Appl.* **2020**, *9*, 201. [CrossRef] [PubMed]

24. Tian, Z.; Shen, C.; Li, J.; Reit, E.; Bachman, H.; Socolar, J.E.S.; Cummer, S.A.; Jun Huang, T. Dispersion tuning and route reconfiguration of acoustic waves in valley topological phononic crystals. *Nat. Commun.* **2020**, *11*, 762. [CrossRef]

25. Zhu, J.; Chen, T.; Chen, C.; Ding, W. Valley Vortex Assisted and Topological Protected Microparticles Manipulation with Complicated 2D Patterns in a Star-like Sonic Crystal. *Materials* **2021**, *14*, 4939. [CrossRef]

26. Fang, W.; Han, C.; Chen, Y.; Liu, Y. Valley Hall Elastic Edge States in Locally Resonant Metamaterials. *Materials* **2022**, *15*, 1491. [CrossRef] [PubMed]

27. Song, X.; Chen, T.; Chen, C.; Ding, W. Observation of frequency band-switchable topological edge modes using a 2 bit coding acoustic topological insulator. *J. Phys. D Appl. Phys.* **2021**, *54*, 255302. [CrossRef]

28. Zhang, Z.; Cheng, Y.; Liu, X. Subwavelength higher-order topological insulator based on stereo acoustic networks. *J. Appl. Phys.* **2021**, *129*, 135101. [CrossRef]

29. Xie, Y.; Wang, W.; Chen, H.; Konneker, A.; Popa, B.I.; Cummer, S.A. Wavefront modulation and subwavelength diffractive acoustics with an acoustic metasurface. *Nat. Commun.* **2014**, *5*, 5553. [CrossRef]

30. Wang, X.; Mao, D.; Li, Y. Broadband acoustic skin cloak based on spiral metasurfaces. *Sci. Rep.* **2017**, *7*, 11604. [CrossRef]

31. Zuo, S.; Wei, Q.; Tian, Y.; Cheng, Y.; Liu, X. Acoustic analog computing system based on labyrinthine metasurfaces. *Sci. Rep.* **2018**, *8*, 10103. [CrossRef] [PubMed]

32. Jia, X.; Yan, M.; Hong, M. Sound energy enhancement via impedance-matched anisotropic metamaterial. *Mater. Des.* **2021**, *197*, 109254. [CrossRef]

33. Orazbayev, B.; Kaina, N.; Fleury, R. Chiral Waveguides for Robust Waveguiding at the Deep Subwavelength Scale. *Phys. Rev. Appl.* **2018**, *10*, 054069. [CrossRef]

34. Li, S.; Yang, J. Topological Transition in Spiral Elastic Valley Metamaterials. *Phys. Rev. Appl.* **2021**, *15*, 014058. [CrossRef]

35. Zhao, R.; Xie, G.-D.; Chen, M.L.N.; Lan, Z.; Huang, Z.; Sha, W.E.I. First-principle calculation of Chern number in gyrotropic photonic crystals. *Opt. Express* **2020**, *28*, 4638–4649. [CrossRef] [PubMed]